Material configurations for *n*-type silicon-based terahertz quantum cascade lasers

A. Valavanis,[*] T. V. Dinh, L. J. M. Lever, Z. Ikonić, and R. W. Kelsall

Institute of Microwaves and Photonics, School of Electronic and Electrical Engineering, University of Leeds, Leeds LS2 9JT, United Kingdom

Silicon-based quantum cascade lasers (QCLs) offer the prospect of integrating coherent terahertz (THz) radiation sources with silicon microelectronics. Theoretical studies have proposed a variety of *n*-type SiGe-based heterostructures as design candidates; however, the optimal material configuration remains unclear. In this work, an optimization algorithm is used to design equivalent THz QCLs in three recently proposed configurations [(001) Ge/GeSi, (001) Si/SiGe, and (111) Si/SiGe], with emission frequencies of 3 and 4 THz. A systematic comparison of the electronic and optical properties is presented. A semiclassical electron transport simulation is used to model the charge carrier dynamics and calculate the peak gain, the corresponding current density, and the maximum operating temperature. It is shown that (001) Ge/GeSi structures yield the best simulated performance at both emission frequencies.

I. INTRODUCTION

Terahertz quantum cascade lasers (THz QCLs) are semiconductor devices in which electrons are transported through a periodic multiple quantum well heterostructure, with a radiative transition in each period.[1] THz QCLs have numerous potential applications including radiation sources for medical and security imaging, and local oscillators in astronomy and remote gas sensing.[2–6]

All THz QCLs to date have been fabricated from III–V compound semiconductors (for example, see Refs. 7 and 8). However, Si-based QCLs could offer a number of significant advantages. Mature Si processing technology may reduce costs and allow integration with conventional electronic devices. Existing THz QCLs operate only at cryogenic temperatures [currently below 186 K for resonant-phonon QCLs (Ref. 7) or 116 K for bound-to-continuum[9]], but the high thermal conductivity of Si-based structures could enable heat to be extracted more effectively and, hence, allow higher operating temperatures. III–V QCLs are also limited to THz emission at frequencies lower than 4.9 THz,[10] owing to the strong absorption in the Reststrahlen band. However, this limitation does not exist in nonpolar group-IV materials.

Although the indirect bandgap in Si has, so far, frustrated efforts to develop an interband laser, this is not an issue for intersubband devices such as QCLs because the radiative transitions occur between subbands within the same valley of an energy band. Midinfrared[11] and THz (Ref. 12) intersubband electroluminescence has been observed from *p*-type SiGe/Si quantum cascade structures. However, dispersion relations for holes in these structures are quite complicated, owing to the contributions from multiple valence bands, and in recent years, attention has switched toward *n*-type structures. This greatly simplifies the device design process and may result in a lower spectral linewidth (and hence greater peak gain) than that of *p*-type structures. Early design proposals included *n*-type Si/SiGe structures that exploited transitions in the Δ valleys of (001) Si quantum wells (QWs), with SiGe barriers.[13] However, a range of alternative material configurations have been considered in recent years. *L* valley transitions in (001)-oriented Ge/GeSi have attracted greatest attention,[14–16] although transitions in the Δ valleys of (111)-

oriented Si/SiGe,[17,18] the Γ valley of Ge/GeSi,[19] and the *L* valleys of Ge/GeSiSn (Ref. 20) have also been considered.

Many properties relating to the bandstructure and carrier transport have a strong effect upon the gain of QCLs. To date, no quantitative comparison has been made of the expected performance of THz QCLs in different Si-based material configurations. In this paper, we present such a comparison by simulating equivalent devices in the (001) Si/SiGe, (111) Si/SiGe, and (001) Ge/GeSi material configurations, using a detailed semiclassical rate-equation approach. Devices emitting near 3 and 4 THz were designed for each material configuration by rescaling a recent bound-to-continuum design,[14] according to the effective mass of the material and then applying an automated design-optimization algorithm. In Sec. II, we calculate the conduction band potentials for each material configuration and the range of energies within QWs that can be used for QCL design. Section III describes our model for simulating carrier transport, gain, and current density in QCLs. The design-optimization algorithm is described in Sec. IV and a summary of the optimized devices is presented. Finally, Sec. V presents a comparison of the simulated performance of devices in each material system.

II. CONDUCTION BAND STATES

A. Model solid approximation

The model solid approximation[25] was used to calculate the conduction band offset between a strained $Si_{1-x}Ge_x$ alloy and a substrate material. The difference between the average of the light-hole, heavy-hole, and spin-orbit split off valence band edges in the two materials was used as a reference energy, as it is almost independent of strain and crystal orientation.[25] The value of this property was interpolated from empirical pseudopotential data as[26]

$$\Delta \overline{E_v} = (0.47 - 0.06 x_s)(x - x_s), \qquad (1)$$

where x_s is the Ge fraction in the substrate. The valence band maximum in an unstrained bulk alloy was found using

$$E_v^{\text{bulk}} = \Delta \overline{E_v} + \tfrac{1}{3} \Delta_{\text{SO}}, \qquad (2)$$

TABLE I. Material parameters for Si and Ge.

Constant	Si	Ge	Unit
a	0.5431[a]	0.5633[a]	nm
Δ_{so}	44.0[b]	296.0[c]	meV
C_{11}	165.773[d]	128.528[d]	GPa
C_{12}	63.924[d]	48.260[d]	GPa
C_{44}	79.619[d]	66.799[d]	GPa
$(\Xi_d + \frac{1}{3}\Xi_u - a_v)^\Delta$	1.72[e]	1.31[e]	eV
$(\Xi_d + \frac{1}{3}\Xi_u - a_v)^L$	−3.12[e]	−2.78[e]	eV
Ξ_u^Δ	9.16[e]	9.42[e]	eV
Ξ_u^L	16.14[e]	15.13[e]	eV

[a]Reference 21.
[b]Reference 22.
[c]Reference 23.
[d]Reference 24.
[e]Reference 25.

where Δ_{SO} is the spin-orbit splitting energy. Material parameters for alloys were found by interpolating from the bulk Si and Ge values in Table I. These parameters yield an offset of 0.55 eV between the top of the valence bands in bulk Ge and Si, which matches a recently measured value for weakly strained Ge and Si films.[27] Very similar parameters have also been shown to yield close agreement with experimental measurements of intersubband absorption energies in Ge/GeSi QWs.[28]

The low-temperature indirect bandgaps for the Δ and L valleys in an unstrained alloy (in eV) were taken as[29]

$$E_g^\Delta = 1.155 - 0.43x + 0.0206x^2,$$
$$E_g^L = 2.010 - 1.270x, \tag{3}$$

and the unstrained conduction band edge for a given valley was found using $E_c^{bulk} = E_v^{bulk} + E_g$.

The effects of hydrostatic and uniaxial strain on the band edge were determined as follows. First, the lattice constant of a thin $Si_{1-x}Ge_x$ layer was found using

$$a(x) = a_{Si}(1 - x) + a_{Ge}x - b_{bow}x(1 - x), \tag{4}$$

where $b_{bow} = 0.2733$ pm (Ref. 21) is a bowing factor.[30] The layer was assumed to deform uniformly, such that the lattice constant matched that of a thick substrate material, a_s. The resulting strain in the plane of epitaxial growth was given by $\varepsilon_\parallel = (a_s - a)/a$.

The hydrostatic deformation was found for each set of conduction band valleys using

$$\Delta E_g^{Hyd} = \left(\Xi_d + \frac{1}{3}\Xi_u - a_v\right) \mathrm{Tr}\,\varepsilon', \tag{5}$$

where $\Xi_d + \frac{1}{3}\Xi_u - a_v$ is the bandgap deformation potential for the Δ or L valleys and $\mathrm{Tr}\,\varepsilon'$ is the trace of the strain tensor, where[31]

$$\mathrm{Tr}\,\varepsilon'^{(001)} = 2\left(1 - \frac{C_{12}}{C_{11}}\right)\varepsilon_\parallel, \tag{6}$$

$$\mathrm{Tr}\,\varepsilon'^{(111)} = \frac{12C_{44}}{C_{11} + 2C_{12} + 4C_{44}}\varepsilon_\parallel, \tag{7}$$

for (001)- and (111)-oriented epilayers, respectively. In the above equations, C_{11}, C_{12}, and C_{44} are elastic constants.

Uniaxial strain leads to splitting of the Δ valley degeneracy in (001)-oriented layers. The energy shifts are given by[31]

$$\Delta E_c^{\Delta_4,Uni} = \frac{1}{3}\Xi_u^\Delta\left(1 + \frac{2C_{12}}{C_{11}}\right)\varepsilon_\parallel,$$
$$\Delta E_c^{\Delta_2,Uni} = -\frac{2}{3}\Xi_u^\Delta\left(1 + \frac{2C_{12}}{C_{11}}\right)\varepsilon_\parallel, \tag{8}$$

for the valleys with their major axes perpendicular and parallel to the growth-direction, respectively, where Ξ_u^Δ is the uniaxial deformation potential for the Δ valleys. Similarly, L valleys in (111)-oriented layers are shifted by

$$\Delta E_c^{L_1,Uni} = -2\Xi_u^L \frac{C_{11} + 2C_{12}}{C_{11} + 2C_{12} + 4C_{44}}\varepsilon_\parallel,$$
$$\Delta E_c^{L_3,Uni} = \frac{2}{3}\Xi_u^L \frac{C_{11} + 2C_{12}}{C_{11} + 2C_{12} + 4C_{44}}\varepsilon_\parallel, \tag{9}$$

for the valley with its major axis in the growth direction, and the three other valleys, respectively. Uniaxial strain has no effect upon the Δ valleys in (111) layers, or the L valleys in (001) layers, owing to symmetry.

Finally, the energy of a given conduction band minimum in a strained layer was found relative to the average substrate valence band using

$$E_c = E_c^{bulk} + \Delta E_g^{Hyd} + \Delta E_c^{Uni}. \tag{10}$$

B. Available energy range

In this section, we determine the energy ranges within group-IV QWs that can be reliably exploited for THz QCL design. It is insufficient to simply calculate the depth of a QW as there are multiple conduction band valleys within the energy range of interest. This can degrade device performance by introducing undesirable intervalley scattering processes. To avoid this problem, we consider the energy difference between the bottom of the well, and the next-lowest conduction band minimum (which may be in either the well or the barrier). This is illustrated in Fig. 1 for the case of a $Si_{0.15}Ge_{0.85}/Ge/Si_{0.15}Ge_{0.85}$ QW on a $Si_{0.025}Ge_{0.975}$ substrate. Here, the L valleys form the bottom of the well and the usable energy range is limited by the Δ_2 valley minima in the barriers.

Figure 2 shows the conduction band minima in QWs that consist of either a Si or Ge well surrounded by SiGe barriers. The energies of the valley minima in the well and barriers are plotted as a function of the barrier alloy composition. In each case, the energies are expressed relative to the bottom of the QW, and usable energy range is therefore given by the lowest line in the plot.

Figure 2(a) shows the results for a (001)-oriented SiGe/Si/SiGe QW. Here, the Δ_2 valleys form the bottom of the well in the Si layer. The total depth of the QW is given by the energy difference between the Δ_2 minima in the barrier and the well. As we shall see in Sec. IV, the barriers in (001)-Si/SiGe QCL designs may need to be thinner than 1 nm, owing to the large Δ_2 quantization effective mass. It is, therefore, necessary to limit the barrier Ge fraction to obtain a lower Δ_2 confinement potential, and hence a realistically wide barrier layer. We selected a $Si_{0.8}Ge_{0.2}$ alloy for the
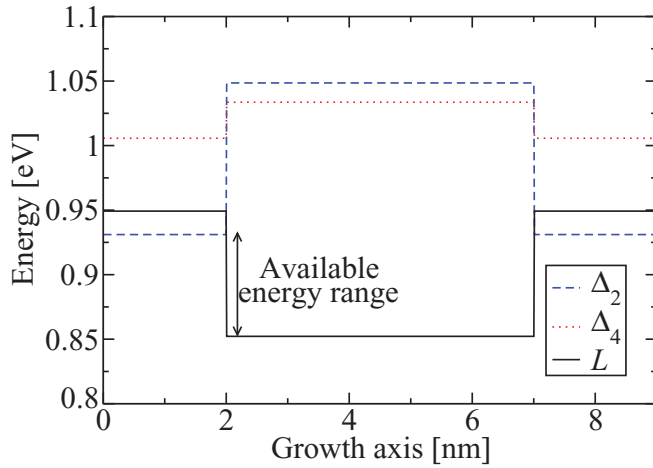
FIG. 1. (Color online) Spatial variation of Δ and L conduction band minima in a $Si_{0.15}Ge_{0.85}/Ge/Si_{0.15}Ge_{0.85}$ heterostructure on a $Si_{0.025}Ge_{0.975}$ virtual substrate. The energy range available for QCL design is defined here as the region between the bottom of the QW and the next-lowest conduction band valley.

barriers, which provides a Δ_2 band offset of 95 meV. A ~4.5% Ge virtual substrate is required for mechanical stability in our (001)-Si/SiGe QCL designs because the Si wells are considerably thicker than the SiGe barrier layers. This induces only a relatively low uniaxial strain in the QW layers and as a result the Δ_4 minima in the barrier layers lie only 5 meV above the bottom of the well. It is, therefore, impossible to avoid the presence of Δ_4 subbands within the energy range of interest for (001) Si/SiGe QCL designs.

Figure 2(b) shows the calculated valley minima for (111)-oriented SiGe/Si/SiGe QWs. Here, the Δ valleys are degenerate, and for most barrier compositions the usable energy range is limited by the Δ valley offset at the Si/SiGe interface. The system is less sensitive to strain, and the maximum usable energy range of 185 meV is obtained when the barriers have a Ge fraction of around 89%. However, our designs in Sec. IV use lower barriers with a $Si_{0.4}Ge_{0.6}$ alloy composition, in order to obtain realistically wide layer widths, as described above. This composition provides a usable energy range of 90 meV.

Figure 2(c) shows the minima for (001)-oriented GeSi/Ge/GeSi QWs. In structures with barrier Ge fractions

greater than around 75%, the L valleys form the bottom of the QW in the Ge layer. However, for lower Ge alloys, the Δ_2 valleys are lowest in energy. The maximum usable energy range of ~90 meV is obtained when the barriers have a Ge fraction of around 0.85. It is worth noting that Δ_2 states in the thin GeSi layers of QCLs will have confinement energies well above the Δ_2 band edge. It may, therefore, be possible to obtain a larger usable energy range by using a lower barrier Ge fraction.

C. Self-consistent Poisson–Schrödinger solution

Self-consistent solutions of the one-dimensional time-independent Schrödinger equation and the Poisson equation were found for the structures considered in this work, using a similar approach to those in Refs. 33 and 34.

The charge density over the length of the structure takes the form $\rho(z) = e[d(z) - \rho_e(z)]$, where e is the electron charge, $d(z)$ is the ionized donor profile, $\rho_e(z)$ is the electron density profile, and z is the spatial position. It was assumed that all donors are ionized, and hence $d(z)$ is equal to the dopant distribution. An initial estimate of the space-charge effect on the Hamiltonian was generated by solving the Poisson equation for a uniform electron distribution, in which $\rho_e(z) \approx N_{2D}/L_p$, where N_{2D} is the sheet doping density across a structural period of length L_p.

A one-band parabolic effective mass approximation was used for the Schrödinger equation, which is justified by the small confinement energy, and the large energy separation from other energy bands. The quantization and density-of-states effective masses (m_q and m_d, respectively) were calculated for each material and crystal orientation using the method in Ref. 32 and are shown in Table II.

Intervalley mixing splits the Δ_2 subbands in (001) Si/SiGe and the L subbands in Ge/GeSi heterostructures. It is, however, only possible to include this effect in complex heterostructures via computationally expensive atomistic approaches such as tight-binding[35] or pseudopotential calculations.[36] We have previously shown that the splitting energies are small in structures wider than 2–3 nm,[36] and have, therefore, omitted the effect in the present work.

Three periods of the conduction band potential profile were used in the Hamiltonian for the QCL simulations, with box
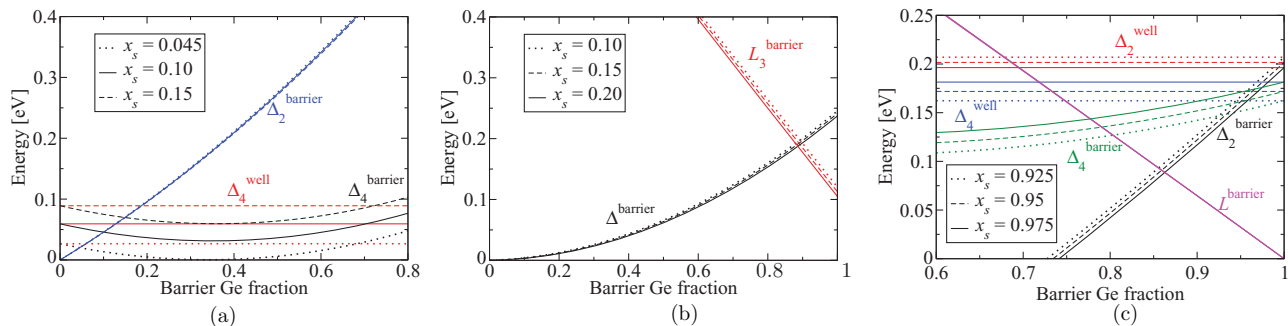

FIG. 2. (Color online) Conduction band minima in the well and barrier regions of Si-based QWs relative to the bottom of the well. Energies are plotted as a function of the barrier alloy composition, and results are shown for structures grown on various $Si_{1-x_s}Ge_{x_s}$ virtual substrates. The figures show band minima in QW heterostructures comprising (a) (001)-SiGe/Si/SiGe, (b) (111)-SiGe/Si/SiGe, and (c) (001)-GeSi/Ge/GeSi.

TABLE II. Quantization and two-dimensional density-of-states effective masses of conduction band valleys in (001) Si, (111) Si, and (001) Ge films, calculated as described in Ref. 32. Masses are expressed relative to the rest mass of a free electron.

Material system	Valley	m_q	m_d
(001) Si	Δ_2	0.916	0.19
(111) Si	Δ	0.26	0.36
(001) Ge	L	0.12	0.30

boundary conditions. This introduced an unrealistic limit to the spatial extent of the wavefunctions which were localized near to the boundaries. To eliminate this effect, we replaced the Schrödinger equation solutions whose wavefunctions lay in the left and right periods of the structure with translated copies of the central period solutions.

Having solved the Schrödinger equation, the subband populations, n_j, were calculated as described in the next section, and a new estimate of the charge distribution was generated, using

$$\rho_e(z) = n_{\text{val}} \sum_j n_j |\psi_j(z)|^2, \quad (11)$$

where n_{val} is the valley degeneracy and ψ_j is the wavefunction of state j. The Poisson and Schrödinger equations were then solved iteratively to find the self-consistent solutions.

III. CARRIER TRANSPORT MODEL

We used a computationally efficient scattering calculation and a semiclassical approach to electron transport in QCLs as described in our previous work.[17,37] Similar Boltzmann- or rate-equation-based models have previously yielded good agreement with experimental data for III–V midinfrared[38] and THz QCLs.[1] Indeed, our carrier-transport model has been shown to calculate the current density and maximum operating temperature quite accurately for a 4.4 THz, seven-well chirped-superlattice GaAs/AlGaAs QCL that is similar in structure to the devices considered in Sec. IV.[39] Although recent work on III–V QCLs has focused on coherent transport effects, using nonequilibrium Green's functions[40] or density matrix[41–46] approaches, the semiclassical approach combines the computational speed and flexibility required for extensive exploration of the parameter space of possible device specifications. We have assumed that coherent transport effects are less significant in the bound-to-continuum devices considered in this work than in resonant-phonon QCLs, owing to the reduced thickness of the injection barriers through which electrons tunnel into the active region. Furthermore, the absence of resonant LO-phonon scattering may lead to longer dephasing times for coherent transport in group-IV materials than in III–V materials.

As in our previous work,[17,37] our model includes elastic intravalley scattering due to interface roughness (allowing arbitrary interface geometries),[37] alloy disorder,[47,48] ionized impurities,[49] electron–electron interactions[50] and deformation potential scattering for electron–acoustic phonon interactions.[51] Intravalley optical phonon interactions are forbidden in Δ valleys due to the symmetry of the system,[52]

but were included for L valleys via a zero-order deformation potential model.[51,53]

Intervalley phonon scattering was also described using the zero-order deformation potential model, with the rates multiplied by the number of equivalent destination valleys. In $L \to L$ scattering, all three destination valleys are degenerate, and separated by a wavevector of the same magnitude. A phenomenological approach, described in Ref. 54, was used to describe the $L \to L$ interactions by treating the combined scattering from all phonon branches as a single interaction. $\Delta \to \Delta$ scattering interactions are categorized as either g type, in which the destination valley lies on the same crystallographic axis as the source, or f type in which the destination valleys lie on a different axis. Phonon energies and deformation potentials for g and f interactions with longitudinal/transverse optical (LO/TO) and acoustic (LA/TA) phonon branches were taken from Ref. 55. The high-energy g-LO, f-LA, and f-TO phonon interactions were determined using the zero-order deformation potential model. The lower energy g-TA, g-LA, and f-TA interactions have no zero-order component in their deformation potential, owing to symmetry selection rules, and were instead determined using a first-order model.[56,57] The bandstructure calculations in Sec. II show that Δ_4 quantum wells correspond to Δ_2 barriers in (001) Si/SiGe heterostructures. The small spatial overlap of wavefunctions leads to very small $\Delta_2 \to \Delta_4$ scattering matrix elements, and f transitions were therefore omitted in our model of (001) devices as a first approximation.

The steady-state populations n_i for each subband were found using a rate-equation approach.[38] Intrasubband scattering rates were typically calculated to be an order of magnitude faster than intersubband scattering. It was therefore assumed that electrons settle between intersubband scattering events to a quasi-thermal Fermi–Dirac distribution. The distribution for each subband was described by a quasi-Fermi energy $E_{F,i}$ and a global electron temperature T_e and the total subband population was found using

$$n_i = \rho^{2D} k_B T_e \ln \left\{ 1 + \exp \left[\frac{E_{F,i}(T_e)}{k_B T_e} \right] \right\}, \quad (12)$$

where $\rho^{2D} = m_d/(\pi \hbar^2)$ is the two-dimensional density-of-states.

A root-finding approach was used to determine the steady-state electron temperature at which no net gain or loss of kinetic energy occurred within the QCL, using the expression[38]

$$\frac{dE_k}{dt} = \sum_f \sum_i n_i(T_e) E_{if} \overline{W}_{if}(T_e) = 0. \quad (13)$$

Here, $\overline{W}_{if}$ is the average intersubband scattering rate between a pair of subbands i and j, summed over all scattering processes, and E_{if} is the energy difference between the subband minima. In the case of inelastic processes, the transition energy was modified as $E_{if} \to E_{if} \pm \hbar \omega_q$ to account for the absorption or emission of a phonon with energy $\hbar \omega_q$.

The current density was estimated by considering the average scattering rates and the change in electron position for all intersubband transitions,[17]

$$J = \frac{e}{L_p} \sum_i n_i n_{\mathrm{val}}^i \sum_f (\langle z \rangle_f - \langle z \rangle_i) \overline{W}_{if}, \qquad (14)$$

where L_p is the length of a structural period of the QCL, n_{val} is the number of equivalent initial valleys, and $\langle z \rangle$ is the expectation position for an electron in a given subband.

The optical gain per unit length was calculated using $G(\omega) = \sigma(\omega)/(\varepsilon_0 c n_r)$,[38,58] where n_r is the real part of the refractive index of the active region stack and σ is the real part of the optical conductivity. This is given by

$$\sigma(\omega) = \frac{\pi e^2}{2 \left(m_q m_d^2 \right)^{\frac{1}{3}} L_p} \sum_{i,j} f_{ji} n_i n_{\mathrm{val}}^i \, \mathrm{sgn}(E_{ij}) L_{ij}(\omega), \qquad (15)$$

where $L_{ij}(\cdot)$ is a lineshape function and $\mathrm{sgn}(\cdot)$ represents the sign function. The oscillator strength is given by

$$f_{ji} = \frac{2 \left(m_q m_d^2 \right)^{\frac{1}{3}}}{\hbar} \omega_{ij} |z_{ij}|^2, \qquad (16)$$

where, $z_{ij} = \langle j|z|i \rangle$ is the dipole matrix element. A Lorentzian lineshape was assumed, with a linewidth of 2 meV, as is typical for the lasing transition in GaAs-based THz QCLs.[9,59]

IV. DEVICE DESIGNS

Equivalent 3 and 4 THz QCLs were designed for each of the three material configurations, in order to simulate the relative performance of each system. To obtain a fair comparison between the materials, all designs were generated using an automated process. In principle, it would have been possible to generate slightly better designs than those presented in this section by manually adjusting the device structures at the start and end of the automated design process. However, we chose not to apply any manual design optimization in this work, in order to ensure that a consistent, reproducible and systematic exploration of the design parameter space was used for each material configuration.

Pure Si or Ge was used as the well material in order to prevent depopulation of the upper laser level via alloy disorder scattering. For each material configuration, a SiGe alloy was chosen for the barriers to maximize the usable energy range (as described in Sec. II), without introducing mechanical instability.

A recent seven-well bound-to-continuum (BTC) (001) Ge/GeSi design was selected as a template for all the designs considered. This device gives a large simulated gain ($\sim$50 cm^{-1}) at 3.5 THz, with a threshold current density around 300 A/cm^2, an operating bias of 3.6 kV/cm,[14] and a maximum operating temperature of 136 K.[60] In this structure, doping was spread evenly over four wells and three barriers in the injector region of each QCL period, with a total sheet density of 8×10^{10} cm^{-2}. Complete donor ionization was assumed. A similar seven-well BTC device has been demonstrated in the GaAs/AlGaAs material system, with an emission frequency of 3.66 THz at an operating bias of 4.15 kV/cm and with a threshold current density of $\sim$200 A/cm at low operating temperatures. This GaAs/AlGaAs device was shown to have a maximum operating temperature of 116 K—the highest reported for a BTC THz QCL.[9]

An automated design algorithm[61] was used to generate a pair of new QCL designs from the Ge/GeSi QCL template, with emission frequencies of 3 and 4 THz. In this method, the gain spectrum was calculated using a range of external electric fields from 3 to 10 kV/cm. The thickness of each barrier and well was adjusted sequentially to maximize the gain in a frequency window of $\pm$200 GHz around the desired emission frequency. The entire process was iterated until the algorithm converged on an optimal layer structure and field. The optimal virtual substrate composition was calculated for each device,[62] to ensure zero net stress across each period of the QCL.

Equivalent 3 and 4 THz QCL designs were generated using (001)- and (111)-oriented Si/SiGe configurations. In each case, the thickness l of each layer in the template QCL structure was transformed according to $l' = l \sqrt{m_q/m_q'}$,[63] where the prime notation denotes parameters of the Si/SiGe system in the appropriate orientation. This transformation yields subband spacings approximately equal to those in the original Ge/GeSi design template. The automated design algorithm was then applied as described above.

Parameters for each of the final QCL designs are summarized in Table III. It can be seen that the Si/SiGe device designs generally require thinner layers than the Ge/GeSi designs, owing to the difference in effective mass. Epitaxial growth of QCLs in Si/SiGe may, therefore, be more challenging. The total length of an active region period is also lower in Ge/GeSi designs than in Si/SiGe, which leads to a lower operating bias. The band structure and electron probability densities for the Ge/GeSi designs are plotted in Fig. 3.

TABLE III. QCL design parameters for each of the devices designed in this work, where f_0 is the emission frequency in THz, x_s denotes the virtual substrate Ge fraction, and F is the operating bias in kV/cm. Bold text in the layer structure represents barriers, while normal weighted text represents wells. Doped layers are underlined.

| Material	f_0	Layers (nm)	x_s	F
(001) Si/Si$_{0.8}$Ge$_{0.2}$	2.9	2.1/**0.8**/6.4/**0.7**/3.5/**1.0**/<u>3.3</u>/**1.2**/<u>3.1</u>/**1.4**/<u>3.0</u>/**1.4**/2.9/**1.6**	0.048	7.1
(111) Si/Si$_{0.4}$Ge$_{0.6}$	3.1	3.2/**1.0**/9.2/**0.8**/5.0/**1.5**/<u>4.5</u>/**1.9**/<u>4.4</u>/**2.3**/<u>4.4</u>/**2.4**/<u>4.2</u>/**3.3**	0.146	6.9
(001) Ge/Ge$_{0.85}$Si$_{0.15}$	3.0	6.7/**1.2**/15.1/**1.4**/11.1/**1.5**/<u>9.5</u>/**1.8**/<u>8.7</u>/**2.3**/<u>7.7</u>/**3.5**/<u>7.1</u>/**4.3**	0.969	3.3
(001) Si/Si$_{0.8}$Ge$_{0.2}$	4.1	2.2/**0.7**/6.1/**0.8**/4.3/**1.0**/<u>3.1</u>/**1.0**/<u>3.1</u>/**1.2**/<u>3.0</u>/**1.4**/2.7/**1.5**	0.045	7.3
(111) Si/Si$_{0.4}$Ge$_{0.6}$	4.0	3.1/**1.0**/8.7/**1.3**/5.3/**1.6**/<u>5.0</u>/**2.0**/<u>4.6</u>/**2.1**/<u>4.0</u>/**2.4**/<u>4.0</u>/**3.7**	0.154	6.9
(001) Ge/Ge$_{0.85}$Si$_{0.15}$	3.8	5.8/**1.0**/15.3/**1.4**/12.3/**1.6**/<u>9.9</u>/**1.9**/<u>8.3</u>/**2.4**/<u>7.8</u>/**2.9**/<u>7.0</u>/**4.3**	0.970	3.5
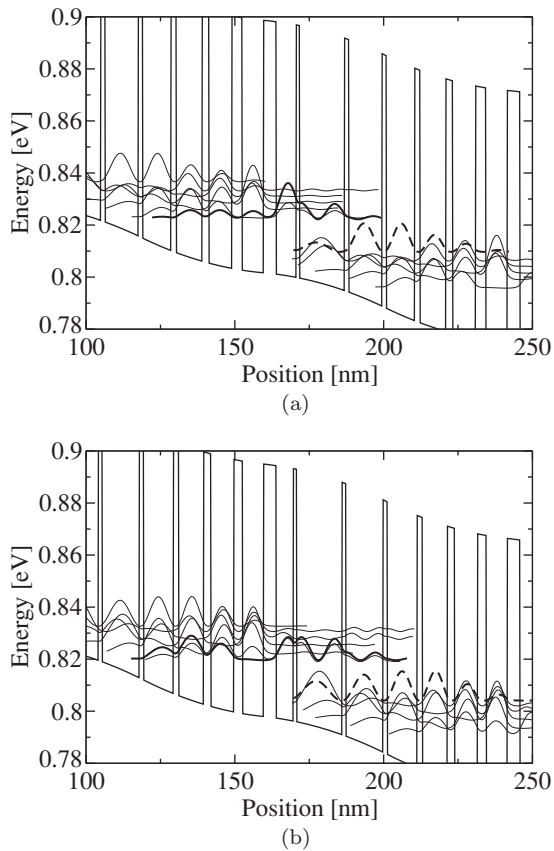
FIG. 3. Potential profile and electron probability densities for optimized (001) Ge/GeSi QCL designs, with emission frequencies and operating biases of (a) 3.0 THz, 3.3 kV/cm and (b) 3.8 THz, 3.5 kV/cm. The upper and lower subbands involved in the radiative transition are shown as solid-bold and dashed-bold lines, respectively.

V. SIMULATED DEVICE PERFORMANCE

The simulated gain spectra for all devices, operating at their respective design biases are shown in Fig. 4. It can be seen that the Ge/GeSi designs yield the highest gain at both frequencies, with peaks of 63 and 82 cm^{-1} for the 3 and 4 THz designs, respectively. The peak gains for the Si/SiGe designs are significantly lower: 25 and 38 cm^{-1} for the (111)-oriented devices, and 5 and 3 cm^{-1} for the (001)-oriented devices at 3 and 4 THz, respectively. We have previously calculated a threshold gain of 31 cm^{-1} for a 15-μm-thick (001) Si/SiGe QCL active region in a copper double-metal waveguide structure.[60] By taking this threshold as an indicative figure, we predict that net gain is achievable for both Ge/GeSi devices, and for the 4 THz (111) Si/SiGe device.

The peak gains in the spectra decrease as the lattice temperature increases, as shown in Fig. 5, owing to the reduction in population inversion. This is caused by a number of thermal effects, including electron leakage from the upper laser level via phonon emission, and by thermal backfilling of the lower laser level. Net gain is predicted for the Ge/GeSi devices up to lattice temperatures of 179 and 184 K for 3 and 4 THz emission, respectively. The 4 THz (111) Si/SiGe device is predicted to yield net gain up to a lattice temperature of 127 K.
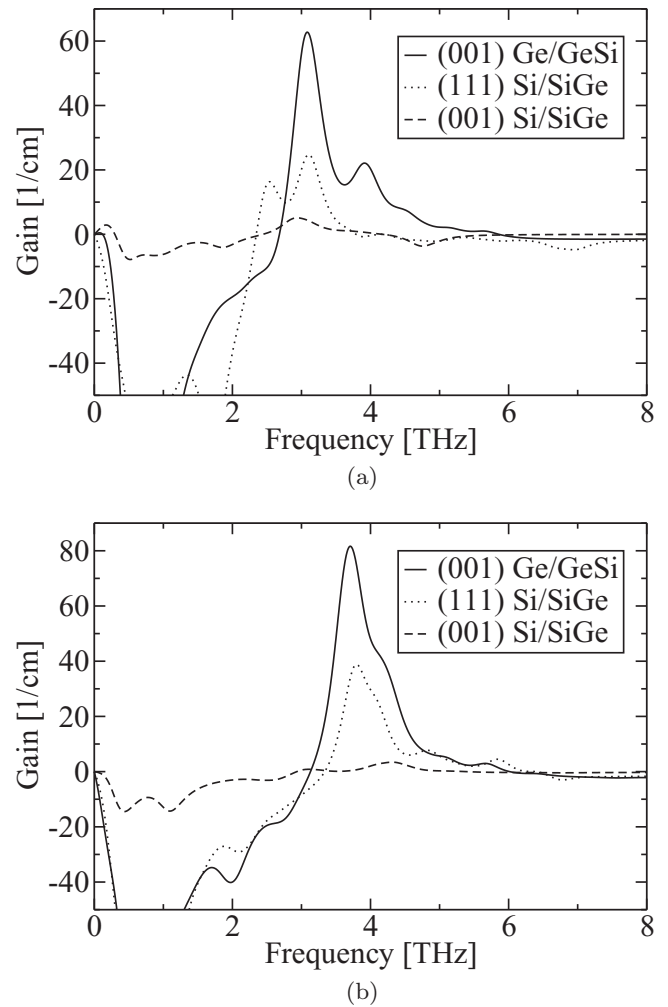

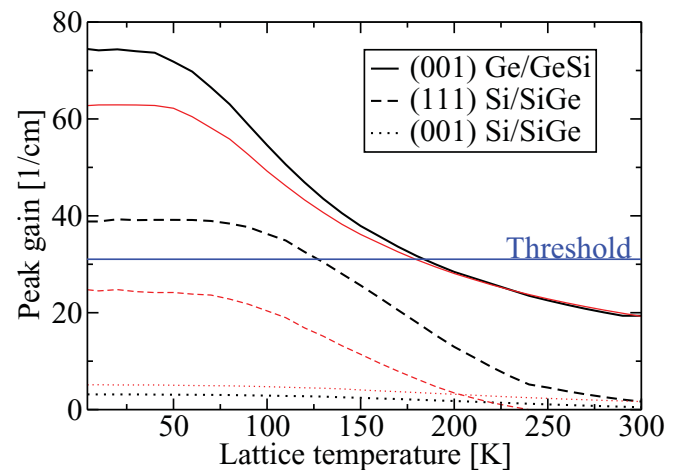FIG. 4. Gain spectra for devices emitting near (a) 3 THz and (b) 4 THz.

FIG. 5. (Color online) Peak gain as a function of lattice temperature for devices emitting near 3 THz (thin lines) and 4 THz (bold lines). The blue line represents an indicative figure of 31 cm^{-1} for the threshold gain.
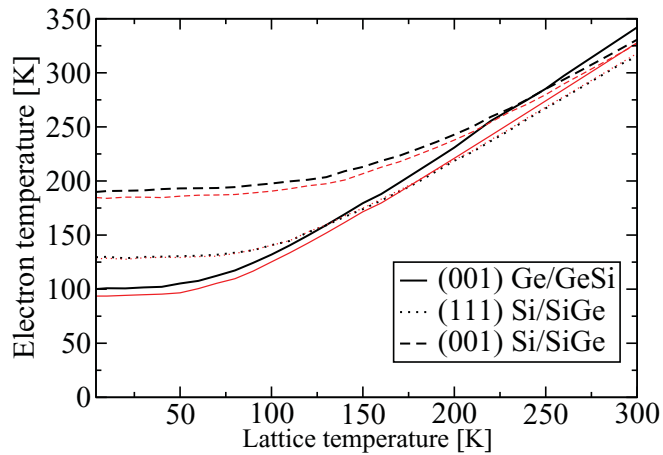
FIG. 6. (Color online) Relationship between electron temperature and lattice temperature for devices emitting near 3 THz (thin lines) and 4 THz (bold lines).

FIG. 7. (Color online) Relationship between peak gain and electron temperature for devices emitting near 3 THz (thin lines) and 4 THz (bold lines).

The simulated temperature of the electron distribution T_e is plotted as a function of lattice temperature T in Fig. 6. At high lattice temperatures, T_e is a linear function of T and is approximately independent of bias. At low lattice temperatures, however, T_e is determined principally by the applied electric field. In the case of (001) Si/SiGe devices, the bias is relatively large (>7 kV/cm), and electrons therefore scatter preferentially into high-energy states. This yields high steady-state electron temperatures of 184 and 189 K for emission at 3 and 4 THz, respectively, at a lattice temperature of 4 K. The electric fields are lower in (111) Si/SiGe and (001) Ge/GeSi devices, owing to the greater lengths of the active regions. This leads to correspondingly lower electron temperatures of 127 and 129 K for (111) Si/SiGe devices, and 93 and 100 K for Ge/GeSi devices emitting at 3 and 4 THz, respectively. The effect of thermal excitation upon device performance is illustrated in Fig. 7. It can be seen that the gain decreases monotonically as electron temperature increases, owing to the thermal backfilling of the lower laser level. Ge/GeSi devices are able to operate with the lowest electron temperatures, and hence achieve the highest peak gains.

The current density was calculated at the design bias for each of the devices. Current densities of 270 and 380 A cm^{-2} were predicted at the design bias for Ge/GeSi devices operating at 3 and 4 THz, respectively. In Si/SiGe, current densities were calculated as 430 and 460 A cm^{-2} for the (111)-oriented devices and 210 and 240 A cm^{-2} for the (001)-oriented devices at 3 and 4 THz, respectively. The low operating currents in (001) Si/SiGe devices were due to the very low scattering rates, which result from the high Δ_2 valley effective mass. The ratio of peak gain to current density was calculated as a figure of merit for each device at its design bias. Ge/GeSi devices were found to have the highest values (240 and 210 cm/kA) followed by (111) Si/SiGe (57 and 84 cm/kA), and (001) Si/SiGe (25 and 14 cm/kA) at 3 and 4 THz, respectively. We should note that our simulations of (001) Si/SiGe QCLs do not include $\Delta_2 \rightarrow \Delta_4$ intervalley scattering events, which would further degrade the predicted performance. However, as these structures already appear to be poor candidates for laser de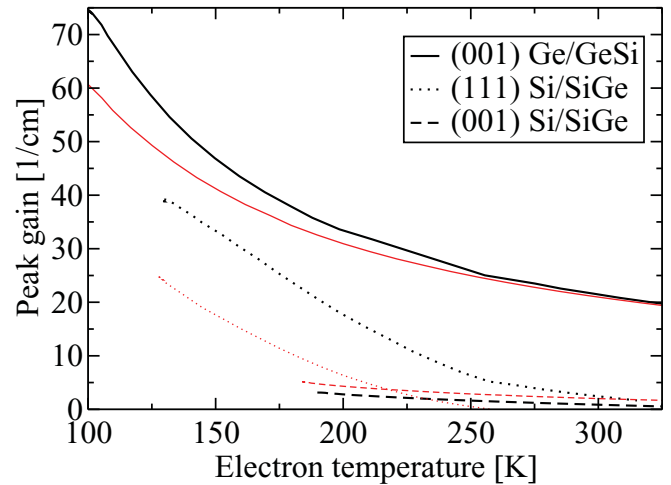sign, a more comprehensive transport model was considered unnec-essary. Threshold current densities were calculated at $T = 4$ K as 440, 210, and 330 A cm^{-2} for the 4 THz (111)-Si/SiGe, 3 THz Ge/GeSi, and 4 THz Ge/GeSi devices, respectively.

VI. CONCLUSION

We have presented a comparison between the simulated performance of Si-based QCLs using the (001) Ge/GeSi, (111) Si/SiGe, and (001) Si/SiGe material configurations. A semiautomated design optimization algorithm was used, in order to provide a fair comparison between equivalent designs. Our results show that (001) Ge/GeSi is the most promising system for development of a Si-based QCL. First, the bandstructure calculations in Sec. II show that the (001) Ge/GeSi and (111) Si/SiGe systems offer a ≳90 meV energy range for QCL design, compared with only ∼5 meV in (001) Si/SiGe systems, owing to the large energy separation between conduction band minima. This reduces the probability of current leakage via intervalley scattering, and allows a wider range of emission frequencies to be targeted. Second, the low *L* valley effective mass was found to yield a relatively long period length for the QCL active region. This reduces the operating electric field, and hence the current density and the temperature of the electron distribution. Net gain was predicted for both of the Ge/GeSi devices, but only one of the four optimized Si/SiGe devices. Ge/GeSi bound-to-continuum QCLs were predicted to operate up to temperatures of 179 and 184 K at 3 and 4 THz, respectively, while the 4 THz (111) Si/SiGe device was predicted to operate up to 127 K. These figures may potentially be improved via waveguide design optimization to minimize losses, or through the use of a resonant-phonon active region design. Nevertheless, the predicted values exceed the highest recorded operating temperature of 116 K for a 3.66 THz seven-well III–V BTC device.[9]

*a.valavanis@leeds.ac.uk

[1]R. Köhler, A. Tredicucci, F. Beltram, H. E. Beere, E. H. Linfield, A. G. Davies, D. A. Ritchie, R. C. Iotti, and F. Rossi, Nature **417**, 156 (2002).

[2]B. S. Williams, Nat. Photonics **1**, 517 (2007).

[3]W. S. Holland, J. S. Greaves, B. Zuckerman, R. A. Webb, C. McCarthy, I. M. Coulson, D. M. Walther, W. R. F. Dent, W. K. Gear, and I. Robson, Nature **392**, 788 (1998).

[4]T. Löffler, T. Bauer, K. Siebert, H. Roskos, A. Fitzgerald, and S. Czasch, Opt. Express **9**, 616 (2001).

[5]M. Califano, N. Q. Vinh, P. J. Phillips, Z. Ikonic, R. W. Kelsall, P. Harrison, C. R. Pidgeon, B. N. Murdin, D. J. Paul, P. Townsend, J. Zhang, I. M. Ross, and A. G. Cullis, Phys. Rev. B **75**, 045338 (2007).

[6]D. Graham-Rowe, Nat. Photonics **1**, 75 (2007).

[7]S. Kumar, Q. Hu, and J. L. Reno, Appl. Phys. Lett. **94**, 131105 (2009).

[8]L. Ajili, G. Scalari, N. Hoyler, M. Giovannini, and J. Faist, Appl. Phys. Lett. **87**, 141107 (2005).

[9]G. Scalari, N. Hoyler, M. Giovannini, and J. Faist, Appl. Phys. Lett. **86**, 181101 (2005).

[10]A. W. M. Lee, Q. Qin, S. Kumar, B. S. Williams, Q. Hu, and J. L. Reno, Appl. Phys. Lett. **89**, 141125 (2006).

[11]G. Dehlinger, L. Diehl, U. Gennser, H. Sigg, J. Faist, K. Ensslin, D. Grützmacher, and E. Müller, Science **290**, 2277 (2000).

[12]S. A. Lynch, R. Bates, D. J. Paul, D. J. Norris, A. G. Cullis, Z. Ikonic, R. W. Kelsall, P. Harrison, D. D. Arnone, and C. R. Pidgeon, Appl. Phys. Lett. **81**, 1543 (2002).

[13]R. W. Kelsall and R. A. Soref, Int. J. High Speed Electron. **13**, 547 (2003).

[14]L. Lever, A. Valavanis, C. A. Evans, Z. Ikonic, and R. W. Kelsall, Appl. Phys. Lett. **95**, 131103 (2009).

[15]K. Driscoll and R. Paiella, Appl. Phys. Lett. **89**, 191110 (2006).

[16]K. Driscoll and R. Paiella, J. Appl. Phys. **102**, 093103 (2007).

[17]A. Valavanis, L. Lever, C. A. Evans, Z. Ikonic, and R. W. Kelsall, Phys. Rev. B **78**, 035420 (2008).

[18]L. Lever, A. Valavanis, Z. Ikonic, and R. W. Kelsall, Appl. Phys. Lett. **92**, 021124 (2008).

[19]G. Han and J. Yu, Semicond. Sci. Technol. **22**, 769 (2007).

[20]G. Sun, H. H. Cheng, J. Menéndez, J. B. Khurgin, and R. A. Soref, Appl. Phys. Lett. **90**, 251105 (2007).

[21]J. P. Dismukes, L. Ekstrom, and R. J. Paff, J. Phys. Chem. **68**, 3021 (1964).

[22]S. Zwerdling, K. J. Button, B. Lax, and L. M. Roth, Phys. Rev. Lett. **4**, 173 (1960).

[23]E. O. Kane, J. Phys. Chem. Solids **1**, 82 (1956).

[24]H. J. McSkimin and P. Andreatch Jr., J. Appl. Phys. **35**, 3312 (1964).

[25]C. G. Van de Walle and R. M. Martin, Phys. Rev. B **34**, 5621 (1986).

[26]M. M. Rieger and P. Vogl, Phys. Rev. B **48**, 14276 (1993).

[27]V. V. Afanas'ev, A. Stesmans, L. Souriau, R. Loo, and M. Meuris, Appl. Phys. Lett. **94**, 172106 (2009).

[28]Y. Busby, M. De Seta, G. Capellini, F. Evangelisti, M. Ortolani, M. Virgilio, G. Grosso, G. Pizzi, P. Calvani, S. Lupi, M. Nardone, G. Nicotra, and C. Spinella, Phys. Rev. B **82**, 205317 (2010).

[29]J. Weber and M. I. Alonso, Phys. Rev. B **40**, 5683 (1989).

[30]D. J. Paul, Semicond. Sci. Technol. **19**, R75 (2004).

[31]S. Smirnov and H. Kosina, Sol. State Electron. **48**, 1325 (2004).

[32]A. Rahman, M. S. Lundstrom, and A. W. Ghosh, J. Appl. Phys. **97**, 053702 (2005).

[33]G. Curatola and G. Iannaccone, Nanotechnology **13**, 267 (2002).

[34]L. R. Ram-Mohan, K. H. Yoo, and J. Moussa, J. Appl. Phys. **95**, 3081 (2004).

[35]M. Virgilio and G. Grosso, Phys. Rev. B **79**, 165310 (2009).

[36]A. Valavanis, Z. Ikonic, and R. W. Kelsall, Phys. Rev. B **75**, 205332 (2007).

[37]A. Valavanis, Z. Ikonic, and R. W. Kelsall, Phys. Rev. B **77**, 075312 (2008).

[38]V. D. Jovanović, S. Höfling, D. Indjin, N. Vukmirović, Z. Ikonic, P. Harrison, J. P. Reithmaier, and A. Forchel, J. Appl. Phys. **99**, 103106 (2006).

[39]D. Indjin, Z. Ikonic, V. D. Jovanović, N. Vukmirović, P. Harrison, and R. W. Kelsall, Semicond. Sci. Technol. **20**, S237 (2005).

[40]S.-C. Lee and A. Wacker, Phys. Rev. B **66**, 245314 (2002).

[41]F. Wang, X. G. Guo, and J. C. Cao, Phys. Rev. B **81**, 045308 (2010).

[42]G. Scalari, C. Walther, M. Fischer, R. Terazzi, H. Beere, D. Ritchie, and J. Faist, Laser and Photon. Rev. **3**, 45 (2009).

[43]H. Callebaut and Q. Hu, J. Appl. Phys. **98**, 104505 (2005).

[44]E. Dupont, S. Fathololoumi, and H. C. Liu, Phys. Rev. B **81**, 205311 (2010).

[45]S. Kumar and Q. Hu, Phys. Rev. B **80**, 245316 (2009).

[46]A. Gordon and D. Majer, Phys. Rev. B **80**, 195317 (2009).

[47]D. N. Quang, N. H. Tung, D. T. Hien, and H. A. Huy, Phys. Rev. B **75**, 073305 (2007).

[48]F. Murphy-Armando and S. Fahy, Phys. Rev. Lett. **97**, 096606 (2006).

[49]T. Unuma, M. Yoshita, T. Noda, H. Sakaki, and H. Akiyama, J. Appl. Phys. **93**, 1586 (2003).

[50]J. H. Smet, C. G. Fonstad, and Q. Hu, J. Appl. Phys. **79**, 9305 (1996).

[51]M. V. Fischetti and S. E. Laux, Phys. Rev. B **48**, 2244 (1993).

[52]B. K. Ridley, *Electrons and Phonons in Semiconductor Multilayers* (Cambridge University Press, Cambridge, 1997).

[53]M. Fischetti, IEEE Trans. Electron Devices **38**, 634 (1991).

[54]C. Jacoboni, F. Nava, C. Canali, and G. Ottaviani, Phys. Rev. B **24**, 1014 (1981).

[55]P. Dollfus, J. Appl. Phys. **82**, 3911 (1997).

[56]D. K. Ferry, Phys. Rev. B **14**, 1605 (1976).

[57]F. Monsef, P. Dollfus, S. Galdin, and A. Bournel, Phys. Rev. B **65**, 212304 (2002); **67**, 059903(E) (2003).

[58]J. H. Davies, *The Physics of Low-Dimensional Semiconductors: An Introduction* (Cambridge University Press, Cambridge, 1998).

[59]C. Walther, G. Scalari, J. Faist, H. Beere, and D. Ritchie, Appl. Phys. Lett. **89**, 231121 (2006).

[60]A. Valavanis, "*n*-type silicon-germanium based terahertz quantum cascade lasers," Ph.D. dissertation (School of Electronic and Electrical Engineering, University of Leeds, 2009) [Available at: http://etheses.whiterose.ac.uk/1262/].

[61]Y. H. Ko and J. S. Yu, Phys. Status Solidi A **207**, 2190 (2010).

[62]P. Harrison, *Quantum Wells, Wires and Dots*, 2nd ed. (Wiley, Chichester, 2005).

[63]A. Valavanis, Z. Ikonic, and R. W. Kelsall, J. Opt. A **11**, 054012 (2009).